NANO LETTERS

pubs.acs.org/NanoLett Letter

Patterned 2D Ferroelectric Perovskite Single-Crystal Arrays for Self-Powered UV Photodetector Boosted by Combining Ferro-Pyro-Phototronic and Piezo-Phototronic Effects

Linjuan Guo,[§] Xiu Liu,[§] Ridong Cong, Linjie Gao, Kai Zhang, Lei Zhao, Xinzhan Wang, Rui-Ning Wang, Caofeng Pan,* and Zheng Yang*

Cite This: *Nano Lett.* 2022, 22, 8241−8249 Read Online

ACCESS | Metrics & More | Article Recommendations | Supporting Information

ABSTRACT: Metal halide perovskite ferroelectrics possess various physical characteristics such as piezoelectric and pyroelectric effects, which could broaden the application of perovskite ferroelectrics and enhance the optoelectronic performance. Therefore, it is promising to combine multiple effects to optimize the performance of the self-powered PDs. Herein, patterned 2D ferroelectric perovskite $(PMA)_2PbCl_4$ microbelt arrays were demonstrated through a PDMS template-assisted antisolvent crystallization method. The perovskite arrays based flexible photodetectors exhibited fine self-powered photodetection performance under 320 nm illumination and much enhanced reproducibility compared with the randomly distributed single-crystal microbelts-based PDs. Furthermore, by introducing the piezo-phototronic effect, the performance of the flexible PD was greatly enhanced. Under an external tensile strain of 0.71%, the responsivity was enhanced by 185% from 84 to 155.5 mA/W. Our findings offer the advancement of comprehensively utilizing various physical characteristics of the ferroelectrics for novel ferroelectric optoelectronics.

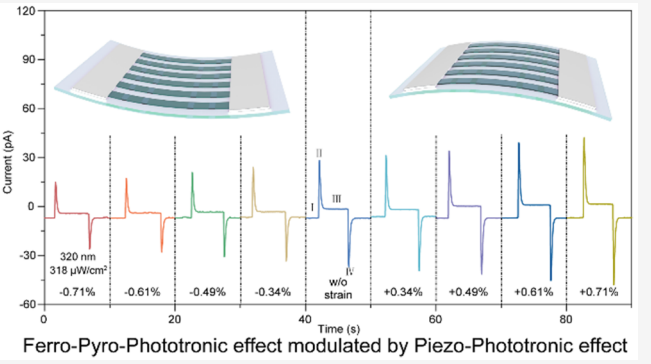

Ferro-Pyro-Phototronic effect modulated by Piezo-Phototronic effect

KEYWORDS: *self-powered UV photodetector, 2D perovskite single-crystal arrays, ferro-pyro-phototronic effect, piezo-phototronic effect*

Ultraviolet (UV) photodetectors (PDs) have shown potential applications in missile alerts, life sciences, and confidential communication due to their high interference immunity.[1−5] Compared with the UV-sensitive wide-band-gap semiconductors like Ga_2O_3,[6−10] wide-band-gap 2D lead-halide perovskites have recently demonstrated extraordinary potential in high-performance PDs due to large absorption coefficients, low trap density, high carrier mobility, and enhanced stability.[11−13] Besides, the structure diversity and tunability of 2D lead-halide perovskites leads to diverse ferroelectrics,[14] such as $(PMA)_2PbCl_4$,[15] $(BA)_2(MA)_2Pb_3Cl_{10}$,[16] and $(EA)_2Pb_3Cl_{10}$.[17] These perovskites with outstanding ferroelectricity and optoelectronic properties are beneficial to fabricate self-powered PDs.[18,19]

Perovskite ferroelectrics also possess piezoelectric effect[20] and pyroelectric effect,[21] which could further boost the perovskite ferroelectrics-based optoelectronic devices.[22] Recently, the light-induced ferro-pyro-phototronic effect has been adopted in ITO/$BaTiO_3$/Ag Schottky junction,[23] $BaTiO_3$/GaN heterojunction,[24] and 2D perovskite single-crystal-based[25,26] UV devices. Moreover, the piezo-phototronic effect provides another effective method to enhance the performance of optoelectronic devices,[27,28] and has attracted much research interest to boost the performance of halide perovskite-based devices.[20,29−32] Thus, by combing the pyro-phototronic and the piezo-phototronic effects, obvious improvements for PEDOT: PSS/ZnO heterojunction[33] and $MAPbI_3$/Si heterojunction-based[34] PDs were observed. Therefore, combing the ferro-pyro-phototronic effect and the piezo-phototronic effect in perovskite ferroelectrics is a promising route to boost the halide perovskite-based PDs' performance.

Nevertheless, until now, a majority of perovskite ferroelectrics-based PDs are fabricated either using monolithic crystals[35,36] or microscale single crystals with random size and orientation,[26] lacking reproducibility and consistency. Patterning of perovskite single crystals is a critical step toward industrial fabrication, which needs high reproducibility and consistency.[37] Therefore, controllable growth of patterned 2D ferroelectric perovskite single-crystal arrays is necessary for creating PDs with enhanced reproducibility.

Received: July 28, 2022
Revised: October 5, 2022
Published: October 10, 2022

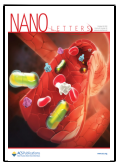

https://doi.org/10.1021/acs.nanolett.2c02978
Nano Lett. 2022, 22, 8241−8249

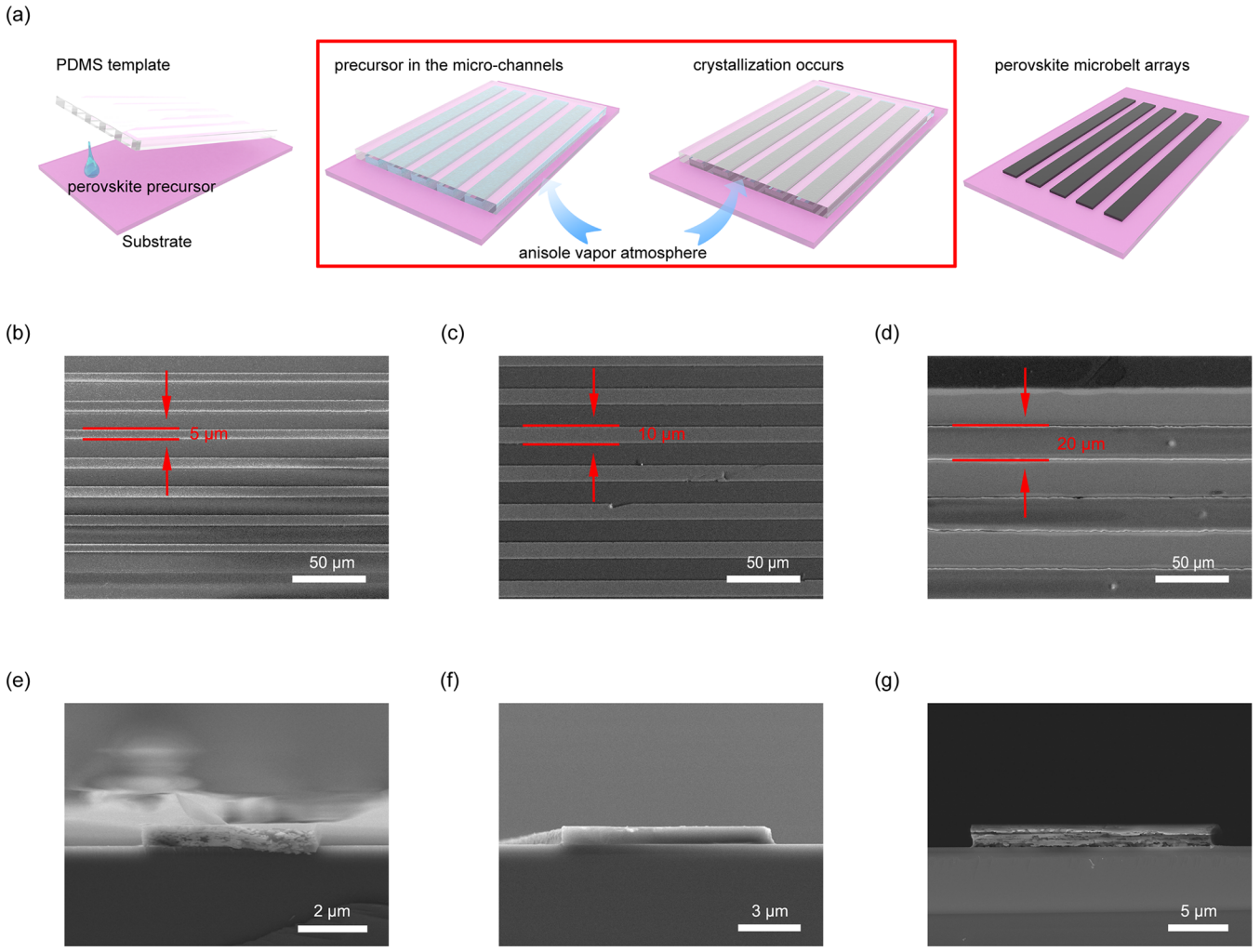

Figure 1. Controllable growth of $(PMA)_2PbCl_4$ SCM arrays. (a) Schematic illustration of the growth of $(PMA)_2PbCl_4$ SCM arrays using the space-confined templated method. (b–d) Top-view SEM images and (e–g) cross-sectional SEM images of the microbelt arrays fabricated with different PDMS microchannel widths, from left to right: 5, 10, and 20 μm.

Herein, we demonstrate patterned 2D ferroelectric perovskite $(PMA)_2PbCl_4$ microbelt arrays based self-powered and flexible UV PDs. The self-powered UV PD exhibited a peak responsivity of 158 mA/W and a fast response time of 73/52 μs. Compared with the random distributed single-crystal microbelts (SCM)-based PDs, the arrays-based PDs exhibited much-improved reproducibility. Furthermore, by introducing the piezo-phototronic effect, the performance of the PD was greatly enhanced. Under an external tensile strain of 0.71%, the responsivity was enhanced by 185% from 84 to 155.5 mA/W. Our results may open new avenues for novel ferroelectric devices.

The space-confined templated method is an effective strategy for the growth of highly patterned perovskite single-crystal arrays.[12,38,39] The patterned $(PMA)_2PbCl_4$ SCM arrays were obtained through a polydimethylsiloxane (PDMS) template-assisted antisolvent crystallization method (Figure 1a). First, PDMS templates with periodic microchannels were obtained by casting the PDMS prepolymer onto the as-prepared SU-8 patterned rectangular arrays. The size of the microchannels in PDMS templates are determined by UV lithography parameters. The top view scanning electron microscope (SEM) images of SU-8 templates and the photographs of the PDMS microchannels are shown in Figure S1a–c and S1d–f, respectively. After being tightly bonded to the substrate, the microchannels will confine the solution and thus limit the growth of the single-crystal arrays. As the anisole vapors diffused into the solution and made it oversaturated, the crystallization occurred within the microchannels. Because of the confining effect of the microchannels, the growth could only continue preferential along the microchannels, leading to aligned direction among different microbelts. After the complete solvent evaporation, the PDMS template was peeled off from the substrate, leaving highly aligned microbelts on the substrate. Since the patterned microchannels in the PDMS template guarantee the aligned growth of perovskite single crystals, the influence of microchannel size on the final products is first studied. The microchannels with different widths of 5, 10, and 20 μm at an identical channel depth of 5 μm are used for comparison. Figure 1b–d and 1e–g present the top-view and cross-sectional SEM images of the $(PMA)_2PbCl_4$ single-crystal arrays obtained with different PDMS microchannel widths. All the $(PMA)_2PbCl_4$ microbelts have monocrystalline natures and smooth surfaces and are free from grain boundaries and surface defects. The cross section of the microbelts shows a rectangle shape, and the width is in good accordance with the microchannels. The thickness of the arrays can be tuned by varying the depth of the microchannels

https://doi.org/10.1021/acs.nanolett.2c02978
Nano Lett. 2022, 22, 8241–8249

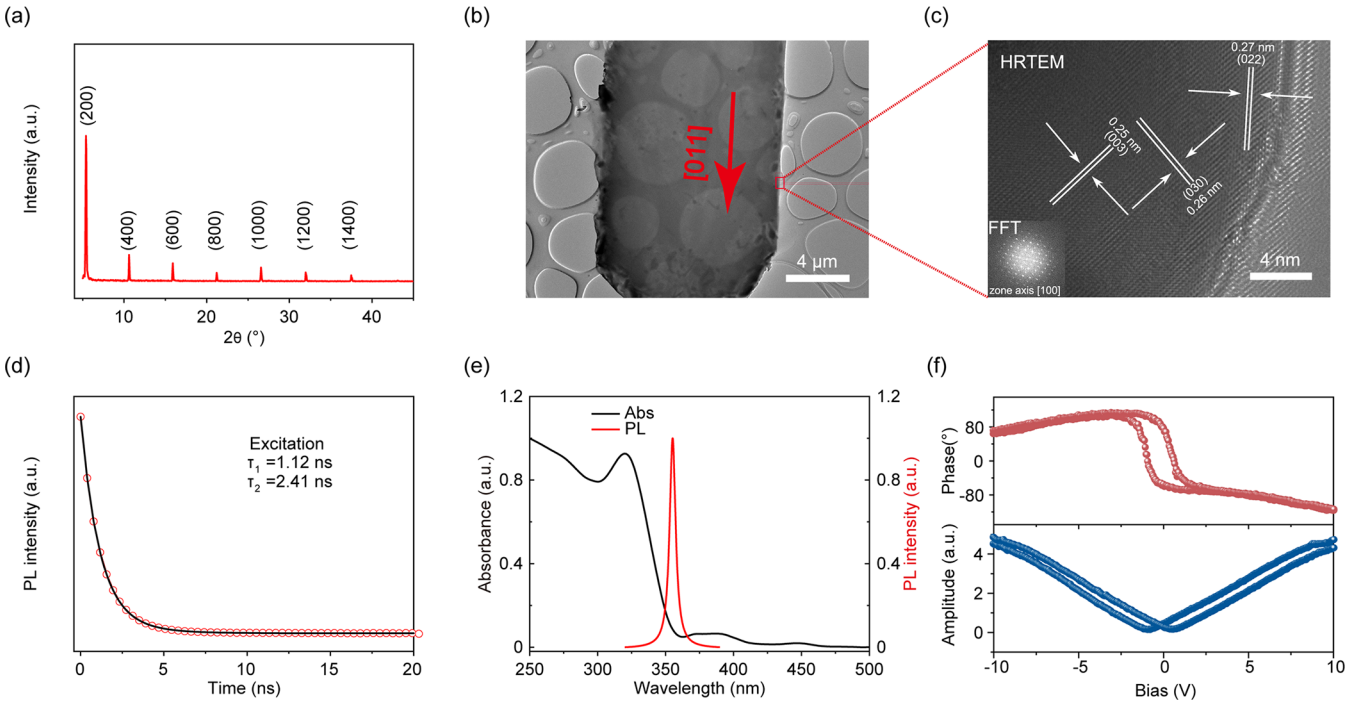

Figure 2. Characterization of the $(PMA)_2PbCl_4$ SCM arrays. (a) XRD pattern of the $(PMA)_2PbCl_4$ SCM arrays. (b) Low-magnified TEM image, (c) HRTEM image and corresponding SAED patterns of a single microbelt (inset) with zone axis along [100]. (d) TRPL spectra and (e) absorption and PL spectra of the $(PMA)_2PbCl_4$ SCM arrays. (f) Lateral PFM hysteresis loops measured in the single microbelt crystal surface (phase signal (up) and amplitude signal (down)).

(depths of 3, 5, and 8 μm at an identical channel width of 10 μm) in PDMS template (Figure S1g–i), with thickness distribution from 710 to 1300 nm (Figure S2a–c).

Figure 2a demonstrates the XRD patterns of the microbelt arrays, showing well-defined, periodically repeated diffraction peaks corresponding to the (h00) (h = 2, 6, 8, ...) crystal planes in $(PMA)_2PbCl_4$ crystalline structure. From the low-magnified transmission electron microscopy (TEM) image in Figure 2b, high-resolution TEM (HRTEM) image, and corresponding selected-area electron diffraction (SAED) patterns in Figure 2c, the orthorhombic crystal structure and the growth direction of the microbelt along [011] can be determined. The energy-dispersive X-ray (EDX) mappings in Figure S3 show the uniform distribution of C, Cs, Pb, and Cl elements. The TRPL spectrum shows a biexponential feature with a bulk recombination lifetime of 2.41 ns and a surface recombination lifetime of 1.12 ns, respectively (Figure 2d). The microbelt arrays have a light absorption cutoff edge located at 360 nm and a sharp PL property with a peak intensity located at about 355 nm (Figure 2e). Trap-state density is another crucial factor that influences the optoelectronic performances of perovskites, which are measured using the SCLC method. From the dark I–V curves in Figure S4, the trap densities for holes and electrons were calculated (Supporting Information) as 3.47×10^9 and 3.76×10^{10} cm^{-3}, respectively. Figure S5 shows the P–E loop of the microbelt arrays along the [011] direction, demonstrating obvious ferroelectric behavior. Furthermore, we performed the lateral piezoresponse force microscopy (PFM) measurements. Figure S6 demonstrates the topographic image of the surface of a single microbelt, showing smooth surface without grain boundaries and pinholes. Distinct hysteresis and butterfly loops are demonstrated with a window bias of ±10 V (Figure 2f), showing the room temperature in plane ferroelectric polarization in the $(PMA)_2PbCl_4$ microbelt, similar to the reported $(PMA)_2PbCl_4$ single crystals.[15] The corresponding amplitude and phase images are shown in Figure S6b,c, which prove the in-plane polarization in the $(PMA)_2PbCl_4$ microbelt. The domains can be distinguished by the different colors, showing different in-plane polarization directions.

Then, the $(PMA)_2PbCl_4$ SCM arrays were transferred onto flexible PEN substrates for the fabricating planar-type flexible UV PDs with Bi/Ag electrode pairs. The schematic transfer and fabrication processes are presented in Figure S7. Before applying strains, the size-dependent (width and thickness) performance of the self-powered PDs were evaluated. The width of the microbelt determines the effective area of the devices, while the thickness determines the carrier transporting distance. First, we measured the performances of the self-powered PDs with arrays widths of 5, 10, and 20 μm and the fixed thickness of ~980 nm (toward 320 nm laser). From the statistical performances from 10 devices plotted in Figure S8a, one can see that the better performances are obtained for PDs with a width of 10 μm. Then, we measured 10 devices with thicknesses in the range of 500–800, 900–1100, and 1200–1400 nm, respectively, with the fixed width of 10 μm. The devices with thickness distribution of 900–1100 nm have better performance than other two kind of devices (Figure S8b). Finally, the optimized width is fixed at 10 μm, and the depth is fixed at 5 μm for PDMS microchannels.

Then, the photoresponses of the flexible PDs without strains were systematically measured (320 nm). Figure 3a shows the schematic diagram of the self-powered PD, with an inset showing the effective illumination area of about 1×10^{-5} cm^2. Figure 3b shows the I–V curves of the device under dark and illumination conditions with power density ranging from 1.59 to 159 $\mu W/cm^2$, respectively. For all conditions, I–V curves clearly show rectifying behavior with an open-circuit voltage (V_{oc}) of about 2 V, making the self-powered detection feasible.

https://doi.org/10.1021/acs.nanolett.2c02978
Nano Lett. 2022, 22, 8241–8249

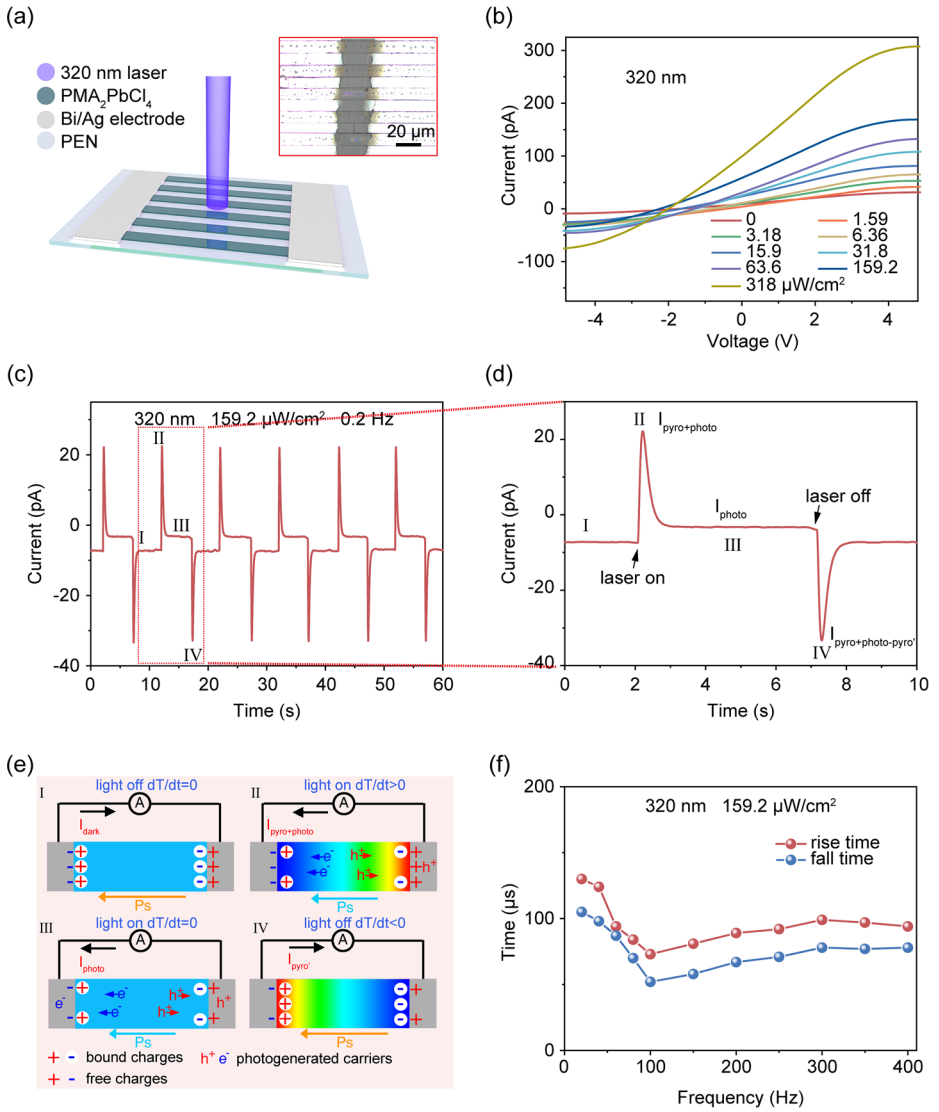

Figure 3. Working mechanism of the flexible $(PMA)_2PbCl_4$ PD. (a) Schematic diagramof the $(PMA)_2PbCl_4$ SCM arrays based PDs on PEN substrate, where the inset denotes the optical image of the devices. (b) $I-V$ curves of the microbelt arrays based PD under dark and 320 nm laser illumination with different power densities. (c) On−off photoresponse of the PD (320 nm, 159.2 $\mu W/cm^2$, 0 V, 0.2 Hz). (d) Enlarged view taken from the marked areas in (c), showing a typical four-stage photoresponse behavior. (e) Schematic working mechanism of the ferro-pyro-phototronic effect based PD. (f) Frequency-dependent response time and recovery time of the self-powered PD.

Typical ferro-pyro-phototronic effect induced four-stage photoresponse behaviors for $(PMA)_2PbCl_4$ photodetector at zero bias are shown in Figure 3c,d. As shown in Figure S9, a positive current pulse appeared when 10.6 μm laser illuminated onto the device. When the temperature decreases, a negative current peak is observed. The current peaks become higher with increased temperature rise rate, with a dT/dt from 8.2 to 16.4 K/s. Besides, Figure S10 shows the $I-t$ characteristics of the PD at forward reversed connected conditions, with opposite current direction. The above two results further prove these current peaks are light-generated pyroelectric signals. The schematic diagrams in Figure 3e and energy band diagrams in Figure S11 schematically demonstrate the mechanism of the current PDs. The temperature rose once the 320 nm laser illuminated on the PD, generating the positive pyroelectric current and photocurrent $I_{pyro+photo}$. Meanwhile, the decrease of the positive ferroelectric polarized charges at the Schottky junction interface leads to the upward bending the energy band diagram, resulting in the decrease of the barrier height. Then, the output current would dramatically decrease and reach a plateau as the temperature remain unchanged, leaving only photocurrent (I_{photo}) originating from photovoltaic effect. When the laser was turned off, temperature fall induced negative pyroelectric current ($I_{pyro'}$) was generated. Finally, the temperature stayed at room temperature without the laser illumination. Thus, the output current returned to dark current. Besides, from frequency-dependent rise/fall time in Figure 3f, one can see that the fastest response speed was obtained with a light switching frequency of 100 Hz. The corresponding response time of the self-powered PD was confirmed as 73 μs for the rise and 52 μs for the fall (159 $\mu W/m^2$) (Figure S12). From the wavelength-dependent responses in Figure S13, it can be seen that the four-stage photoresponse behaviors were obvious for light illumination with different wavelengths (159.2 $\mu W/cm^2$), with the maximum response located at 320 nm. The performances of the PDs are highly influenced by the polarization voltage. When less than 0.8 V,

https://doi.org/10.1021/acs.nanolett.2c02978
Nano Lett. 2022, 22, 8241−8249

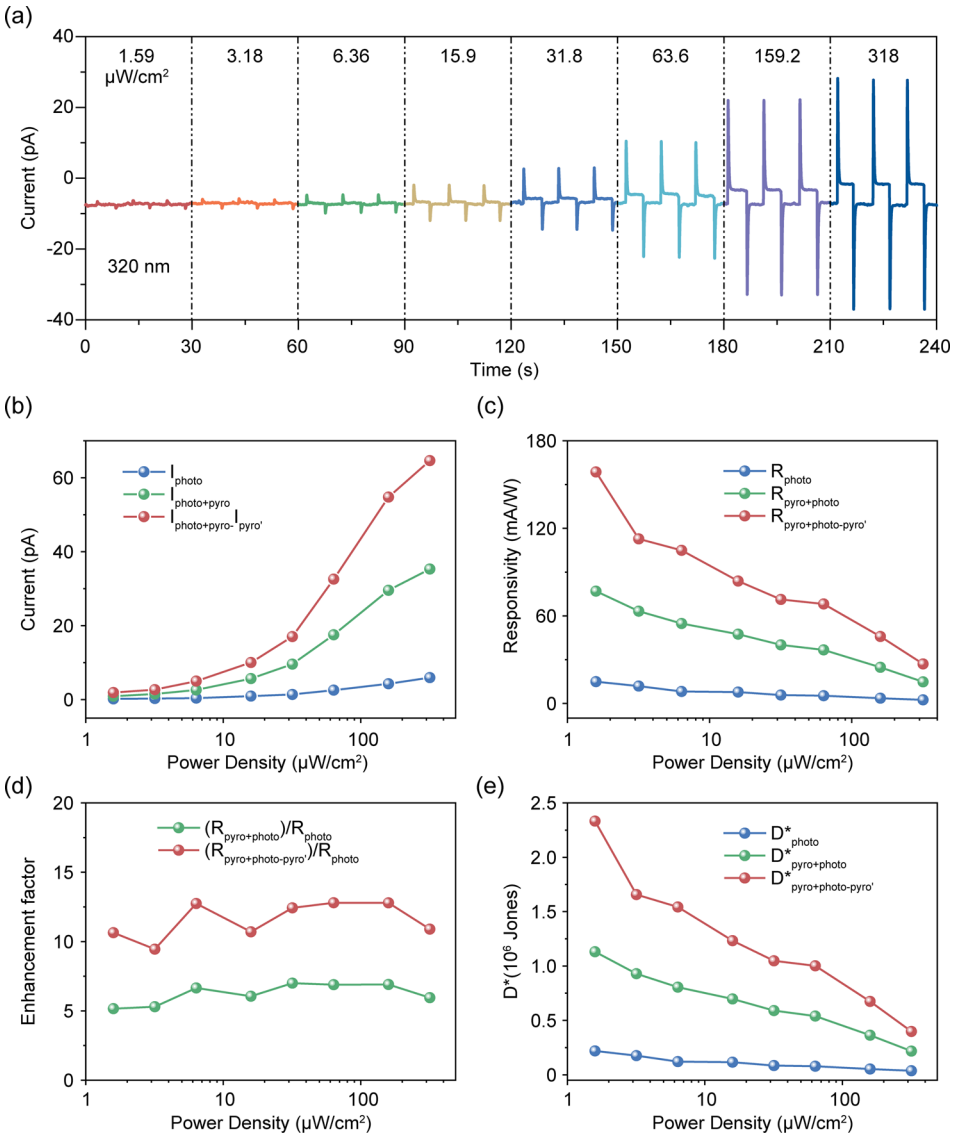

Figure 4. UV photoresponse performances of the $(PMA)_2PbCl_4$ PD under 320 nm laser illumination at zero bias. (a) $I-t$ curves of the PD with different power densities from 1.59 to 318 $\mu W/cm^2$. (b) I_{photo}, $I_{pyro+photo}$, and $I_{pyro+photo}-I_{pyro'}$, (c) corresponding R_{photo}, $R_{pyro+photo}$, and $R_{pyro+photo-pyro'}$, (d) corresponding enhancement factor ($R_{pyro+photo}/R_{photo}$ and $R_{pyro+photo-pyro'}/R_{photo}$), and corresponding D^*_{photo}, $D^*_{pyro+photo}$, and $D^*_{pyro+photo-pyro'}$ of the self-powered PD as a function of power density.

the pyroelectric currents increase with the rise of the polarization voltage, with a saturation at 1 V (Figure S14).

The on−off $I-t$ photoresponses of the PD (320 nm, 1.59−318 $\mu W/cm^2$, 0 V) were recorded and plotted in Figure 4a, all showing stable four-stage photoresponses. Then, power density-based relative peak-to-peak output current ($I_{pyro+photo}-I_{pyro'}$), $I_{pyro+photo}$, and I_{photo} in Figure 4a are plotted in Figure 4b. All the three output currents increase with the increase of power density.

The noise spectral density of the PDs was caculated from the dark current shown in Figure S15a at zero bias and estimated to be $\sim 3.3\times 10^{-16}$ $A/Hz^{1/2}$ at the bandwidth of 1 Hz using a fast Fourier transform method according to the literature (Figure S15b).[40] The corresponding responsivity (R) and specific detectivity (D^*) are calculated (with equations shown in the Supporting Information) and summarized in Figure 4c,e. As shown in Figure 4d, for different power densities, the R is greatly improved by the ferro-pyro-phototronic effect. The peak $R_{pyro+photo-pyro'}$ value is 158 mA/W (1.59 $\mu W/cm^2$). The corresponding D^* is 2.3×10^6 Jones (cm $Hz^{1/2}/W$). Furthermore, we analyzed the reproducibility of the PDs made from microbelt arrays and randomly oriented microbelts. Figure S16a−d show the averaged photodetecting performances of the two kinds of devices. Although the average maximum responsivity of the PDs based on random oriented microbelts is several times higher than the arrays-based ones, the arrays-based ones show much improved reproducibility.

Then, the influence of the piezo-phototronic effect was systematically investigated by applying different tensile and compressive strains under 320 nm laser illumination. The external strains were applied by bending the PEN substrates using a manual moving stage (Figure 5a). Since the microbelt arrays are fixed by the PMMA layer, the upper and downward bending of the substrates will lead to the stretch and compression of arrays, respectively. The corresponding strain estimation method is conducted according to our early reported result,[31] with the procedure in Figure S17. First, the influences of the strains on the charge carrier transport

https://doi.org/10.1021/acs.nanolett.2c02978
Nano Lett. 2022, 22, 8241−8249

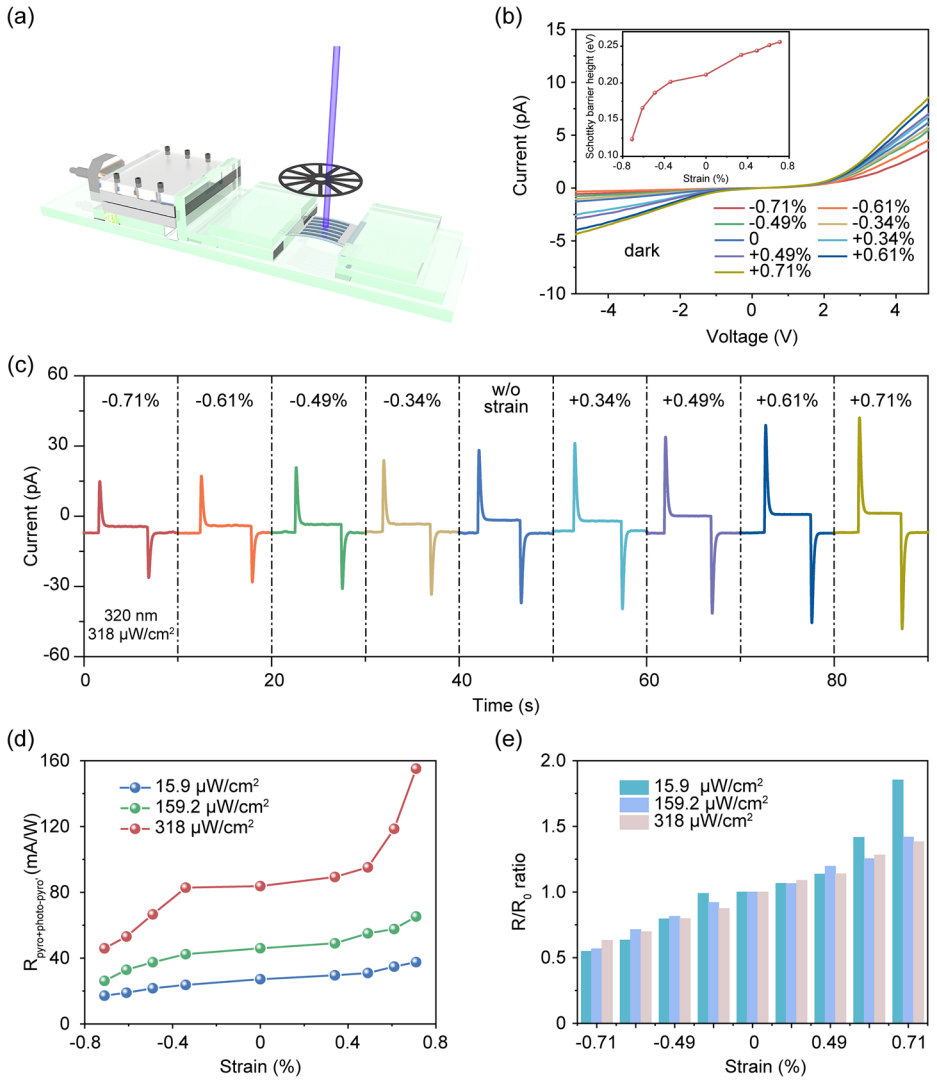

Figure 5. Piezo-phototronic effect modulated performance of the flexible $(PMA)_2PbCl_4$ PD. (a) Schematic illustration of the experimental setup showing how strains are applied. (b) $I-V$ characteristics of the self-powered PD at dark condition under different strains varying from −0.71 to 0.71%. Inset: calculated corresponding SBH of the PD as a function of the externally applied strain. (c) Photoresponses of the PD under 325 nm laser illumination (318 $\mu W/cm^2$) with different strains, showing the modulation effect of the pyro-phototronic effect. (d) $R_{pyro+photo-pyro'}$ and (e) responding strain dependence of enhancement ratio of $R_{pyro+photo-pyro'}$ as a function of applied tensile strain with incident light power density of 15.9, 159.2, and 318 $\mu W/cm^2$, respectively.

characteristics of the Schottky junction are analyzed by measuring the dark $I-V$ curves of the PD with different strains ranging from −0.71 to 0.71% (Figure 5b). One can see that the dark current increases with the increase of tensile strain and decreases with the increase of compressive strain both at reversed bias and forward bias. This phenomenon is different from the $I-V$ characterizations of traditional piezoelectric materials under strains[27] since the reversed bias can overturn the direction of ferroelectric polarization. The Schottky barrier height (SBH) is then derived from the dark $I-V$ curves and plotted in the inset of Figure 5b. The SBH increases from 0.123 eV at a compressive strain of −0.71% to 0.211 eV (no strain) and further increases to 0.256 eV at a tensile strain of 0.71%, indicating effective modulating function to the SBH through piezo-electronic effect. Therefore, the carrier transport behaviors at the Schottky junction can be tuned by varying the applied strains. The modulation effect of the piezo-phototronic effect on the photocurrent illuminated condition $I-V$ curves was also evident (Figure S18). Then, the photoresponses of the PD toward 320 nm laser with different power densities under different tensile and compressive strains were tested and plotted in Figures 5c and S19, respectively. Both the pyroelectric current and photocurrent increase with the increase of tensile strain and decrease with the increase of compressive strain. The corresponding strain-modulated $R_{pyro+photo-pyro'}$ and R/R_0 ratio are shown in Figure 5d,e, respectively, in which R_0 is the initial R without strain. Under a tensile strain of 0.71%, $R_{pyro+photo-pyro'}$ at a power density of 15.9 $\mu W/cm^2$ can be enhanced from 84 to 155.5 mA/W and decreased to 46.9 mA/W under a compressive strain of −0.71%. For the other two power densities (159 and 318 $\mu W/cm^2$), a similar trend could be found. The highest responsivity enhancement ratio can reach up to 185% under the tensile strain of 0.71% at a lower power density (15.9 $\mu W/cm^2$). The strain-modulated R_{photo} in Figure S20a shows a similar trend as a function of strain. Then, $I_{pyro+photo}-I_{pyro'}$, enhancement factor, and $R_{pyro+photo-pyro'}$ are calculated, summarized, and plotted for each power density and externally applied strain in Figure

https://doi.org/10.1021/acs.nanolett.2c02978
Nano Lett. 2022, 22, 8241−8249

S20b–d. It is evident that the output current and the enhancement factor increase monotonously as the increase of strain from 0.71 to −0.71%. The tensile strains have a positive impact on the ferro-pyro-phototronic effect. However, for our PDs, the piezo-phototronic effect has little effect on the response speed (Figure S21). Our PDs also demonstrated great mechanical stability, humidity stability and long-term stability. The mechanical stability of the flexible PD was evaluated by comparing the photoresponses before and after multiple bend-release cycles under the same laser illumination intensity. The normalized $I_{pyro+photo}-I_{pyro'}$ almost keeps unchanged after 1000 bending cycles (Figure S22). The unencapsulated PDs underwent a 25% of performance decay after being stored in a constant temperature and humidity chamber (85 ± 5% RH at RT) for 8 days (Figure S23). In addition, the unencapsulated device maintained 71.7% of the initial responses after being exposed to the open environment (45 ± 10% RH at RT) for more than 70 days (Figure S24).

Furthermore, the working mechanism of the piezo-phototronic effect on the photoresponses under tensile and compressive strains are systematically analyzed (Figure S25). According to our early report, a Schottky contact will be formed between $(PMA)_2PbCl_4$ microbelts and the Bi/Ag electrodes. When the light is absorbed by the perovskite arrays, electron–hole pairs are separated and driven by the built-in electric field, generating the photocurrents. Moreover, the light-induced temperature rise will lead to the generation of the pyroelectric currents. Since the electric field poling was applied before photoresponse measurements, the polarization direction was clear. When the tensile strain is applied, positive piezoelectric polarization charges will be generated at the Schottky junction interface, attracting the electrons moving toward and repelling the holes away from the Schottky contact, leading to the downward bending of the band edge at the interface, lifting the SBH, beneficial for the transport and collection of charge carriers, resulting in the enhancement of the photocurrent. Meanwhile, the piezo-charges at the interface by tensile strain are consistent with the ferroelectric-induced bound charges. Therefore, the effective positive pyro-potential is increased and the ferro-pyro-phototronic effect induced output current is enhanced. On the contrary, the compressive strain will generate negative polarization charges at the Schottky interface, resulting in the reduced SBH, and decrease of the separation efficiency of photogenerated carriers. Additionally, the leakier barrier makes the charge carriers directly crossing the interface easier, leading to weakened pyroelectric currents.[41] Therefore, the above experimental results and energy band diagram show that the piezo-phototronic effect can effectively modulate the ferro-pyro-phototronic effect.

In summary, we had successfully prepared 2D ferroelectric $(PMA)_2PbCl_4$ SCM arrays-based self-powered PDs. Based on ferro-pyro-electric effect, the PDs show great photoresponse toward 320 nm laser, with much-improved reproducibility. Furthermore, the piezo-phototronic effect was introduced to further enhance the PD's performances, with an enhancement of over 185% for pyroelectric photocurrent. This work provides in-depth understanding of utilization of multiple effects of perovskite ferroelectrics to fully enhance the performances of perovskite ferroelectrics-based PDs.

■ ASSOCIATED CONTENT

Supporting Information

The Supporting Information is available free of charge at https://pubs.acs.org/doi/10.1021/acs.nanolett.2c02978.

Experimental section of the whole process; equations of trap-state density, responsivity and specific detectivity; SEM images, optical image, height distribution, EDS analysis, $P-E$ loops, PFM measurements of 2D ferroelectric $(PMA)_2PbCl_4$ microbelt arrays; statistical performances, energy band diagrams, temporal response, wavelength-dependent photoresponse, $I-V$ characteristics, $I-t$ curves, dark current analysis, and stability of devices (PDF)

■ AUTHOR INFORMATION

Corresponding Authors

Caofeng Pan − *CAS Center for Excellence in Nanoscience, Beijing Institute of Nanoenergy and Nanosystems, Chinese Academy of Sciences, Beijing 100083, PR China;* orcid.org/0000-0001-6327-9692; Email: cfpan@binn.cas.cn

Zheng Yang − *Hebei Key Laboratory of Optic-Electronic Information and Materials, National & Local Joint Engineering Laboratory of New Energy Photoelectric Devices, College of Physics Science and Technology, Hebei University, Baoding 071002, PR China;* orcid.org/0000-0001-7172-4717; Email: yangzheng06@hbu.edu.cn

Authors

Linjuan Guo − *Hebei Key Laboratory of Optic-Electronic Information and Materials, National & Local Joint Engineering Laboratory of New Energy Photoelectric Devices, College of Physics Science and Technology, Hebei University, Baoding 071002, PR China*

Xiu Liu − *Hebei Key Laboratory of Optic-Electronic Information and Materials, National & Local Joint Engineering Laboratory of New Energy Photoelectric Devices, College of Physics Science and Technology, Hebei University, Baoding 071002, PR China*

Ridong Cong − *Hebei Key Laboratory of Optic-Electronic Information and Materials, National & Local Joint Engineering Laboratory of New Energy Photoelectric Devices, College of Physics Science and Technology, Hebei University, Baoding 071002, PR China*

Linjie Gao − *Hebei Key Laboratory of Optic-Electronic Information and Materials, National & Local Joint Engineering Laboratory of New Energy Photoelectric Devices, College of Physics Science and Technology, Hebei University, Baoding 071002, PR China*

Kai Zhang − *Hebei Key Laboratory of Optic-Electronic Information and Materials, National & Local Joint Engineering Laboratory of New Energy Photoelectric Devices, College of Physics Science and Technology, Hebei University, Baoding 071002, PR China*

Lei Zhao − *Hebei Key Laboratory of Optic-Electronic Information and Materials, National & Local Joint Engineering Laboratory of New Energy Photoelectric Devices, College of Physics Science and Technology, Hebei University, Baoding 071002, PR China;* orcid.org/0000-0001-9226-2929

Xinzhan Wang − *Hebei Key Laboratory of Optic-Electronic Information and Materials, National & Local Joint*

https://doi.org/10.1021/acs.nanolett.2c02978
Nano Lett. 2022, 22, 8241−8249

Engineering Laboratory of New Energy Photoelectric Devices, College of Physics Science and Technology, Hebei University, Baoding 071002, PR China

Rui-Ning Wang − *Hebei Key Laboratory of Optic-Electronic Information and Materials, National & Local Joint Engineering Laboratory of New Energy Photoelectric Devices, College of Physics Science and Technology, Hebei University, Baoding 071002, PR China*

Complete contact information is available at: https://pubs.acs.org/10.1021/acs.nanolett.2c02978

Author Contributions

[§]L.G. and X.L. contributed equally to this work. Z. Y. conceived and supervised the project. L. G. and X. L. synthesized the perovskites and measured the optoelectronic properties. R. C contributed to the fabrication of the devices. K. Z. contributed to the temporal response measurement. L. Z. contributed to the ferroelectric measurement. X. W. contributed to the PL measurement. R. W. calculated the SBH. L. G. wrote the manuscript. Z. Y. and L. G. modified it. S. W. and C. F. provided funding support and critical suggestions for this work. All the authors reviewed the manuscript.

Notes

The authors declare no competing financial interest.

■ ACKNOWLEDGMENTS

This work was supported by the National Natural Science Foundation of China (Grant Nos. 62005072, 62104057, 51972094, 52125205, U20A20166, 61805015, and 61804011), the Natural Science Foundation of Hebei Province (Grant Nos. E2020201025, E2021201016, and B2021201034), Hebei Education Department (Grant No. BJK2022050), the Advanced Talents Incubation Program of the Hebei University (521000981287, 521000981351, and 521000981248), the Science and Technology Plan Project of Hebei Province (Grant No. 226Z1002G).

■ REFERENCES

(1) Li, S.; Zhang, Y.; Yang, W.; Liu, H.; Fang, X. 2D Perovskite $Sr_2Nb_3O_{10}$ for High-Performance UV Photodetectors. *Adv. Mater.* **2020**, *32*, 1905443.

(2) Zhang, Y.; Zhao, X.; Chen, J.; Li, S.; Yang, W.; Fang, X. Self-Polarized $BaTiO_3$ for Greatly Enhanced Performance of ZnO UV Photodetector by Regulating the Distribution of Electron Concentration. *Adv. Funct. Mater.* **2020**, *30*, 1907650.

(3) Zhao, R.; Ma, N.; Song, K.; Yang, Y. Boosting Photocurrent via Heating $BiFeO_3$ Materials for Enhanced Self-Powered UV Photodetectors. *Adv. Funct. Mater.* **2020**, *30*, 1906232.

(4) Ning, Y.; Zhang, Z.; Teng, F.; Fang, X. Novel Transparent and Self-Powered UV Photodetector Based on Crossed ZnO Nanofiber Array Homojunction. *Small* **2018**, *14*, 1703754.

(5) Ouyang, W. X.; Teng, F.; Fang, X. S. High Performance BiOCl Nanosheets/TiO_2 Nanotube Arrays Heterojunction UV Photodetector: The Influences of Self-Induced Inner Electric Fields in the BiOCl Nanosheets. *Adv. Funct. Mater.* **2018**, *28*, 1707178.

(6) Guo, D.; Su, Y.; Shi, H.; Li, P.; Zhao, N.; Ye, J.; Wang, S.; Liu, A.; Chen, Z.; Li, C.; Tang, W. Self-Powered Ultraviolet Photodetector with Superhigh Photoresponsivity (3.05 A/W) Based on the GaN/Sn:Ga_2O_3 pn Junction. *ACS Nano* **2018**, *12*, 12827−12835.

(7) Xie, C.; Lu, X.-T.; Tong, X.-W.; Zhang, Z.-X.; Liang, F.-X.; Liang, L.; Luo, L.-B.; Wu, Y.-C. Recent Progress in Solar-Blind Deep-Ultraviolet Photodetectors Based on Inorganic Ultrawide Bandgap Semiconductors. *Adv. Funct. Mater.* **2019**, *29*, 1806006.

(8) Dubey, A.; Mishra, R.; Hsieh, Y.-H.; Cheng, C.-W.; Wu, B.-H.; Chen, L.-J.; Gwo, S.; Yen, T.-J. Aluminum Plasmonics Enriched Ultraviolet GaN Photodetector with Ultrahigh Responsivity, Detectivity, and Broad Bandwidth. *Adv. Sci.* **2020**, *7*, 2002274.

(9) Song, W.; Chen, J.; Li, Z.; Fang, X. Self-Powered MXene/GaN van der Waals Heterojunction Ultraviolet Photodiodes with Superhigh Efficiency and Stable Current Outputs. *Adv. Mater.* **2021**, *33*, 2101059.

(10) Peng, Y.; Lu, J.; Wang, X.; Ma, W.; Que, M.; Chen, Q.; Li, F.; Liu, X.; Gao, W.; Pan, C. Self-powered high-performance flexible GaN/ZnO heterostructure UV photodetectors with piezo-phototronic effect enhanced photoresponse. *Nano Energy* **2022**, *94*, 106945.

(11) Tsai, H.; Nie, W.; Blancon, J. C.; Stoumpos, C. C.; Asadpour, R.; Harutyunyan, B.; Neukirch, A. J.; Verduzco, R.; Crochet, J. J.; Tretiak, S.; et al. High-efficiency two-dimensional Ruddlesden-Popper perovskite solar cells. *Nature* **2016**, *536*, 312−316.

(12) Feng, J.; Gong, C.; Gao, H.; Wen, W.; Gong, Y.; Jiang, X.; Zhang, B.; Wu, Y.; Wu, Y.; Fu, H.; Jiang, L.; Zhang, X. Single-crystalline layered metal-halide perovskite nanowires for ultrasensitive photodetectors. *Nat. Electron.* **2018**, *1*, 404−410.

(13) Liang, C.; Gu, H.; Xia, Y.; Wang, Z.; Liu, X.; Xia, J.; Zuo, S.; Hu, Y.; Gao, X.; Hui, W.; Chao, L.; Niu, T.; Fang, M.; Lu, H.; Dong, H.; Yu, H.; Chen, S.; Ran, X.; Song, L.; Li, B.; Zhang, J.; Peng, Y.; Shao, G.; Wang, J.; Chen, Y.; Xing, G.; Huang, W. Two-dimensional Ruddlesden-Popper layered perovskite solar cells based on phase-pure thin films. *Nature Energy* **2021**, *6*, 38−45.

(14) Xu, H.; Han, S.; Sun, Z.; Luo, J. Recent Advances of Two-dimensional Organic-Inorganic Hybrid Perovskite Ferroelectric Materials. *Acta Chim. Sinica* **2021**, *79*, 23−35.

(15) Liao, W. Q.; Zhang, Y.; Hu, C. L.; Mao, J. G.; Ye, H. Y.; Li, P. F.; Huang, S. D.; Xiong, R. G. A lead-halide perovskite molecular ferroelectric semiconductor. *Nat. Commun.* **2015**, *6*, 7338.

(16) Xu, Z.; Weng, W.; Li, Y.; Liu, X.; Yang, T.; Li, M.; Huang, X.; Luo, J.; Sun, Z. 3D-to-2D Dimensional Reduction for Exploiting a Multilayered Perovskite Ferroelectric toward Polarized-Light Detection in the Solar-Blind Ultraviolet Region. *Angew. Chem., Int. Ed. Engl.* **2020**, *59*, 21693−21697.

(17) Wang, S.; Li, L.; Weng, W.; Ji, C.; Liu, X.; Sun, Z.; Lin, W.; Hong, M.; Luo, J. Trilayered Lead Chloride Perovskite Ferroelectric Affording Self-Powered Visible-Blind Ultraviolet Photodetection with Large Zero-Bias Photocurrent. *J. Am. Chem. Soc.* **2020**, *142*, 55−59.

(18) Cao, F.; Tian, W.; Wang, M.; Cao, H.; Li, L. Semitransparent, Flexible, and Self-Powered Photodetectors Based on Ferroelectricity-Assisted Perovskite Nanowire Arrays. *Adv. Funct. Mater.* **2019**, *29*, 1901280.

(19) Ye, H.; Peng, Y.; Shang, X.; Li, L.; Yao, Y.; Zhang, X.; Zhu, T.; Liu, X.; Chen, X.; Luo, J. Self-Powered Visible-Infrared Polarization Photodetection Driven by Ferroelectric Photovoltaic Effect in a Dion-Jacobson Hybrid Perovskite. *Adv. Funct. Mater.* **2022**, *32*, 2200223.

(20) Ding, R.; Lyu, Y.; Wu, Z.; Guo, F.; Io, W. F.; Pang, S. Y.; Zhao, Y.; Mao, J.; Wong, M. C.; Hao, J. Effective Piezo-Phototronic Enhancement of Flexible Photodetectors Based on 2D Hybrid Perovskite Ferroelectric Single-Crystalline Thin-Films. *Adv. Mater.* **2021**, *33*, 2101263.

(21) Ji, C.; Wang, S.; Li, L.; Sun, Z.; Hong, M.; Luo, J. The First 2D Hybrid Perovskite Ferroelectric Showing Broadband White-Light Emission with High Color Rendering Index. *Adv. Funct. Mater.* **2019**, *29*, 1805038.

(22) Shahrokhi, S.; Gao, W.; Wang, Y.; Anandan, P. R.; Rahaman, M. Z.; Singh, S.; Wang, D.; Cazorla, C.; Yuan, G.; Liu, J. M.; Wu, T. Emergence of Ferroelectricity in Halide Perovskites. *Small Methods* **2020**, *4*, 2000149.

(23) Zhao, K.; Ouyang, B.; Bowen, C. R.; Yang, Y. Enhanced photocurrent via ferro-pyro-phototronic effect in ferroelectric $BaTiO_3$ materials for a self-powered flexible photodetector system. *Nano Energy* **2020**, *77*, 105152.

(24) Zhang, Y.; Chen, J.; Zhu, L.; Wang, Z. L. Self-Powered High-Responsivity Photodetectors Enhanced by the Pyro-Phototronic

Effect Based on a $BaTiO_3$/GaN Heterojunction. *Nano Lett.* **2021**, *21*, 8808−8816.
(25) Liu, Y.; Pan, X.; Liu, X.; Han, S.; Wang, J.; Lu, L.; Xu, H.; Sun, Z.; Luo, J. Tailoring Interlayered Spacers of Two-Dimensional Cesium-Based Perovskite Ferroelectrics toward Exceptional Ferro-Pyro-Phototronic Effects. *Small* **2022**, *18*, 2106888.
(26) Guo, L.; Liu, X.; Gao, L.; Wang, X.; Zhao, L.; Zhang, W.; Wang, S.; Pan, C.; Yang, Z. Ferro-Pyro-Phototronic Effect in Monocrystalline 2D Ferroelectric Perovskite for High-Sensitive, Self-Powered, and Stable Ultraviolet Photodetector. *ACS Nano* **2022**, *16*, 1280−1290.
(27) Wu, W.; Wang, L.; Li, Y.; Zhang, F.; Lin, L.; Niu, S.; Chenet, D.; Zhang, X.; Hao, Y.; Heinz, T. F.; Hone, J.; Wang, Z. L. Piezoelectricity of single-atomic-layer MoS_2 for energy conversion and piezotronics. *Nature* **2014**, *514*, 470−474.
(28) Han, X.; Du, W.; Yu, R.; Pan, C.; Wang, Z. L. Piezo-Phototronic Enhanced UV Sensing Based on a Nanowire Photodetector Array. *Adv. Mater.* **2015**, *27*, 7963−7969.
(29) Lai, Q.; Zhu, L.; Pang, Y.; Xu, L.; Chen, J.; Ren, Z.; Luo, J.; Wang, L.; Chen, L.; Han, K.; Lin, P.; Li, D.; Lin, S.; Chen, B.; Pan, C.; Wang, Z. L. Piezo-phototronic Effect Enhanced Photodetector Based on $CH_3NH_3PbI_3$ Single Crystals. *ACS Nano* **2018**, *12*, 10501−10508.
(30) Pan, Z.; Peng, W.; Li, F.; He, Y. Piezo-Phototronic Effect on Performance Enhancement of Anisotype and Isotype Heterojunction Photodiodes. *Adv. Funct. Mater.* **2018**, *28*, 1706897.
(31) Yang, Z.; Jiang, M.; Guo, L.; Hu, G.; Gu, Y.; Xi, J.; Huo, Z.; Li, F.; Wang, S.; Pan, C. A high performance $CsPbBr_3$ microwire based photodetector boosted by coupling plasmonic and piezo-phototronic effects. *Nano Energy* **2021**, *85*, 105951.
(32) Jang, C. W.; Kim, H.; Nazeeruddin, M. K.; Shin, D. H.; Choi, S.-H. Piezo-electric and -phototronic effects of perovskite 2D|3D heterostructures. *Nano Energy* **2021**, *84*, 105899.
(33) Peng, W.; Wang, X.; Yu, R.; Dai, Y.; Zou, H.; Wang, A. C.; He, Y.; Wang, Z. L. Enhanced Performance of a Self-Powered Organic/Inorganic Photodetector by Pyro-Phototronic and Piezo-Phototronic Effects. *Adv. Mater.* **2017**, *29*, 1606698.
(34) Yang, Z.; Wang, H.; Guo, L.; Zhou, Q.; Gu, Y.; Li, F.; Qiao, S.; Pan, C.; Wang, S. A Self-Powered Photodetector Based on $MAPbI_3$ Single-Crystal Film/n-Si Heterojunction with Broadband Response Enhanced by Pyro-Phototronic and Piezo-Phototronic Effects. *Small* **2021**, *17*, 2101572.
(35) Ji, C.; Dey, D.; Peng, Y.; Liu, X.; Li, L.; Luo, J. Ferroelectricity-Driven Self-Powered Ultraviolet Photodetection with Strong Polarization Sensitivity in a Two-Dimensional Halide Hybrid Perovskite. *Angew. Chem., Int. Ed. Engl.* **2020**, *59*, 18933−18937.
(36) Li, L.; Liu, X.; Li, Y.; Xu, Z.; Wu, Z.; Han, S.; Tao, K.; Hong, M.; Luo, J.; Sun, Z. Two-Dimensional Hybrid Perovskite-Type Ferroelectric for Highly Polarization-Sensitive Shortwave Photodetection. *J. Am. Chem. Soc.* **2019**, *141*, 2623−2629.
(37) Han, X.; Wu, W.; Chen, H.; Peng, D.; Qiu, L.; Yan, P.; Pan, C. Metal Halide Perovskite Arrays: From Construction to Optoelectronic Applications. *Adv. Funct. Mater.* **2021**, *31*, 2005230.
(38) Yang, Z.; Lu, J.; ZhuGe, M.; Cheng, Y.; Hu, J.; Li, F.; Qiao, S.; Zhang, Y.; Hu, G.; Yang, Q.; Peng, D.; Liu, K.; Pan, C. Controllable Growth of Aligned Monocrystalline $CsPbBr_3$ Microwire Arrays for Piezoelectric-Induced Dynamic Modulation of Single-Mode Lasing. *Adv. Mater.* **2019**, *31*, 1900647.
(39) Sun, Y.; Liu, X.; Deng, W.; Zhang, X.; Lu, Z.; Chang, Z.; Fang, X.; Wu, D.; Jie, J. A Three-Dimensional Confined Crystallization Strategy Toward Controllable Growth of High-Quality and Large-Area Perovskite Single Crystals. *Adv. Funct. Mater.* **2022**, *32*, 2112758.
(40) Liu, C. H.; Chang, Y. C.; Norris, T. B.; Zhong, Z. Graphene photodetectors with ultra-broadband and high responsivity at room temperature. *Nat. Nanotechnol.* **2014**, *9*, 273−278.
(41) Yang, M. M.; Luo, Z. D.; Mi, Z.; Zhao, J.; E, S. P.; Alexe, M. Piezoelectric and pyroelectric effects induced by interface polar symmetry. *Nature* **2020**, *584*, 377−381.

https://doi.org/10.1021/acs.nanolett.2c02978
Nano Lett. 2022, 22, 8241−8249